Spin-noise spectroscopy of a spin-one system

S. Liu, P. Neveu, J. Delpy, E. Wu, Fabien Bretenaker, F. Goldfarb

Spin noise spectroscopy of a spin-one system

S. Liu,[1,2] P. Neveu,[1] J. Delpy,[1] E. Wu,[2] F. Bretenaker,[1] and F. Goldfarb[1,3]

[1] *Université Paris-Saclay, CNRS, Ecole Normale Supérieure Paris-Saclay, CentraleSupélec, LuMIn, Orsay, France*
[2] *East China Normal University, State key laboratory of precision spectroscopy, Shanghai, China*
[3] *Institut Universitaire de France (IUF)*

The spin noise mechanisms in a spin-1 system are theoretically and experimentally investigated in details. Eight different independent spin degrees of freedom are isolated, leading to spin noise signals at the Larmor frequency or its second harmonic in the presence of a magnetic field. The signature of these different modes of the detuned probe light beam polarization fluctuations, observed either as Faraday rotation noise or as ellipticity noise, are shown to depend dramatically on the probed transition. In particular, depending on the Zeeman structure of the upper level of the transitions, the different noise modes can be visible or not, and their dependence on the probe polarization can be completely modified. Those predictions are successfully compared with measurements of spin noise signals using three different transitions of an ensemble of metastable ^{4}He at room temperature.

I. INTRODUCTION

It has been known for decades that noise correlations can provide a non-perturbative method to characterize a system [1]. In the 1980s in particular, it was suggested that information on a spin ensemble might be extracted from its spontaneous spin noise [2, 3]. More than two decades later, benefiting from the development of spectrum analysis equipment and lasers, spin noise spectroscopy (SNS) has gained much more interest and has demonstrated its usefulness in various systems [4–7]. Compared to traditional optical detection methods, recent developments of the SNS technique can give access to more information such as, for example, the possibility to resolve very close optical transitions, to determine the transition broadening type, homogeneous or inhomogeneous, or to unveil spin interactions among several species [8–11].

However, these results are usually described as if they had been performed with a spin-1/2 system, which can lead only to conventional orientation noise for the linearly polarized probe laser [12–14]. Systems with a spin higher than 1 can exhibit much richer SNS signals such as ellipticity noise, which can give rise to polarization dependent resonances at both the Larmor and twice the Larmor frequencies [15–17]. High spin systems are ubiquitous and used in many applications in modern quantum technologies [18–21]: understanding their dynamics and the corresponding spontaneous noise can thus have both fundamental and technological interests. Such investigations are nevertheless complicated by the hyperfine structure of the alkali atoms that are often used in SNS studies performed in atom vapors. In this context, metastable ^{4}He appears as an ideal toy model because i) as a spin one system it is ideal for the study of spin systems larger than 1/2, ii) it has optical transitions easy to probe with near-infrared lasers, and iii) it exhibits three different transitions with different degeneracies for the upper level, which are sufficiently separated to be probed independently.

Using the three well separated $J = 1 \to J = 0$, $J = 1 \to J = 1$, and $J = 1 \to J = 2$ transitions available in metastable ^{4}He, we can thus emphasize the role of the structure of the upper level of the probed transition and provide a complete understanding of the SNS of a spin-1 system. To reach this goal, we first theoretically describe the different spin degrees of freedom that can exist in spin-1 systems, and show that 8 modes can be isolated similarly to the 8 multipole moments precessions already studied in earlier works [22]. We can then shine a new light on the results obtained with the simplest of the three transitions, namely the so-called D_0 $J = 1 \to J = 0$, which has already been the subject of experimental investigations [17]. We indeed explain how the different noise modes map to the two types of available optical detection: either the detection of the fluctuations in the orientation of the probe light polarization – so-called Faraday rotation noise – or the detection of the fluctuations in the ellipticity induced on the probe light – so-called ellipticity noise. We then investigate how these two types of noises, related respectively to circular and linear birefringence of the atomic sample, evolve with the experimental conditions. These predictions are compared with measurements in metastable ^{4}He.

We then generalize this approach to more complicated situations, namely the D_1 $J = 1 \to J = 1$ and D_2 $J = 1 \to J = 2$ transitions, in which the upper level has respectively three and five Zeeman sublevels. This allows to predict the conditions in which the different noise modes can be detected, in particular the dependence of the different SNS signals on the probe polarization orientation in the different detection schemes. These predictions are compared with extensive measurements, allowing one to understand the influence of the structure of the upper level of the transition and going well beyond the oversimplified spin-1/2 model.

II. SPIN-1 NOISE MODES

This section discusses the various noise processes in a spin-1 system and their dynamic evolution under the influence of a transverse magnetic field. The way these different noises can be optically detected and the corresponding spectra are discussed in the following sections.

In the context of spin noise studies where one observes the fluctuations of the system around its thermal equilibrium state, the density matrix of a spin one system can be written as the sum of two parts: the

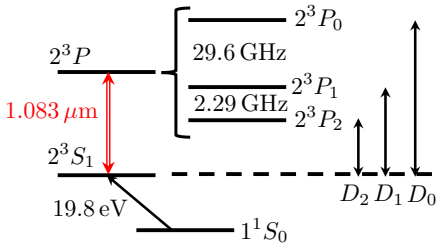

Figure 1. Level structure of ^{4}He. The three transitions D_0, D_1, and D_2 from the metastable 2^3S_1 level are well separated, by a difference larger than the 0.8 GHz Doppler broadening at room temperature.

thermal equilibrium state and the fluctuations around this thermal equilibrium state [23]:

$$\rho = \frac{1}{3}\hat{\mathbb{1}} + \frac{1}{2}\sum_{i=1}^{8} \lambda_i \hat{M}_i \ . \tag{1}$$

In this equation the fluctuations are expanded over the spin operators $\hat{M}_i$, $i = 1..8$, of a single particle, with coefficients $\lambda_i \equiv \mathrm{Tr}[\rho \hat{M}_i]$. These generalize the Pauli matrices, in the sense that the $\hat{M}_i$'s are traceless Hermitian operators, and obey the orthogonality relation $\mathrm{Tr}(\hat{M}_i \hat{M}_j) = 2\delta_{ij}$. With the quantization axis along z, i.e. in a basis consisting in the three kets $\{|-1\rangle_z, |0\rangle_z, |1\rangle_z\}$, the first three operators $\hat{M}_1, \hat{M}_2, \hat{M}_3$ describe the polarization of the spin along the directions z, x, and y, respectively:

$$\hat{M}_1 = \begin{bmatrix} 1 & 0 & 0 \\ 0 & 0 & 0 \\ 0 & 0 & -1 \end{bmatrix} \ , \tag{2}$$

$$\hat{M}_2 = \frac{1}{\sqrt{2}} \begin{bmatrix} 0 & 1 & 0 \\ 1 & 0 & 1 \\ 0 & 1 & 0 \end{bmatrix} \ , \tag{3}$$

$$\hat{M}_3 = \frac{1}{\sqrt{2}} \begin{bmatrix} 0 & -i & 0 \\ i & 0 & -i \\ 0 & i & 0 \end{bmatrix} \ . \tag{4}$$

The five remaining operators are represented by the following matrices:

$$\hat{M}_4 = \begin{bmatrix} 0 & 0 & 1 \\ 0 & 0 & 0 \\ 1 & 0 & 0 \end{bmatrix} \ , \quad \hat{M}_5 = \begin{bmatrix} 0 & 0 & -i \\ 0 & 0 & 0 \\ i & 0 & 0 \end{bmatrix} \ , \tag{5}$$

$$\hat{M}_6 = \frac{1}{\sqrt{2}} \begin{bmatrix} 0 & 1 & 0 \\ 1 & 0 & -1 \\ 0 & -1 & 0 \end{bmatrix} \ , \quad \hat{M}_7 = \frac{1}{\sqrt{2}} \begin{bmatrix} 0 & -i & 0 \\ i & 0 & i \\ 0 & -i & 0 \end{bmatrix} \ , \tag{6}$$

$$\hat{M}_8 = \frac{1}{\sqrt{3}} \begin{bmatrix} 1 & 0 & 0 \\ 0 & -2 & 0 \\ 0 & 0 & 1 \end{bmatrix} \ . \tag{7}$$

The operators $\hat{M}_4, \hat{M}_5$ describe coherences between the spin states $|-1\rangle_z$ and $|+1\rangle_z$, while $\hat{M}_6$ and $\hat{M}_7$ describe coherences between $|0\rangle_z$ and the states $|\pm 1\rangle_z$. Finally $\hat{M}_8$ describes the spin alignment corresponding to population imbalance between $|0\rangle_z$ and the other two states. As discussed by Colangelo & al [23], these tensors are spin independent but corresponds to polarization moments in the case of a spin 1 [22].

The fluctuations of the spin system at thermal equilibrium correspond to the appearance of non zero random values for the coefficients λ_i at random instants. In a typical SNS experiment, a weak magnetic field is always introduced to shift the spin noise resonance frequency from DC where technical noises are dominant. Therefore, each time one of the processes $\hat{M}_i$ is excited, it further evolves under the influence of this magnetic field. We consider here a magnetic field B_x oriented along the x direction, orthogonal to the propagation direction of the probe light. The evolution is then governed by the Hamiltonian $\hat{H} = \hbar\omega_L B_x \hat{M}_2$, where ω_L is the Larmor frequency associated to the $^3S_1$ state. The density operator $\rho(t)$ thus evolves from $t = 0$ to t according to

$$\rho(t) = \hat{U}(t)\rho(0)\hat{U}^\dagger(t) = \frac{1}{3}\hat{\mathbb{1}} + \frac{1}{2}\Sigma_i \lambda_i \hat{U}(t)\hat{M}_i\hat{U}^\dagger(t) \ , \tag{8}$$

where the evolution operator $\hat{U}(t)$ is given by

$$\hat{U}(t) = \exp\left[-i\frac{\hat{H}t}{\hbar}\right] \ . \tag{9}$$

As we want to isolate and characterize the oscillation modes of the system, we do not consider here any relaxation processes. However, they are included in the simulations, which are shown in a previous article and in the next sections [17]. In order to understand the observations of SNS signals in different experimental conditions, it is instructive to observe the evolution of every component $\hat{U}(t)\hat{M}_i\hat{U}^\dagger(t)$ for $i = 1..8$. We thus successively take $\lambda_i \neq 0$ for $i = 1..8$ at $t = 0$ and compute the subsequent evolution of ρ. The results are reproduced in Fig. 2. For example, the first frame in Fig. 2 corresponds to $i = 1$. To make the evolution easier to visualize, we take the exaggerated value $\lambda_1 = 2/3$, which is much larger than the noise amplitudes actually observed in the experiment. The initial state at $t = 0$ is then

$$\rho(0) = \frac{1}{3}\hat{\mathbb{1}} + \frac{1}{3}\hat{M}_1 = \begin{bmatrix} \frac{2}{3} & 0 & 0 \\ 0 & \frac{1}{3} & 0 \\ 0 & 0 & 0 \end{bmatrix} \ . \tag{10}$$

The first frame in Fig. 2 then represents the evolution of this density operator with time at different instants between $t = 0$ and $t = 2\pi/\omega_L$. Since the non-diagonal elements of the density matrix are complex, we choose here to plot only the moduli of the density matrix elements.

Figure 2 shows that the different initial states, labeled $i = 1..8$, lead to very different types of evolution. For some of them, populations ($i = 1, 3$) oscillate at the Larmor frequency ω_L while some others ($i = 4, 5, 6, 7, 8$) oscillate at $2\omega_L$. The case $i = 2$ corresponds to the spin aligned along x, which is an eigenstate of $\hat{H}$ and thus does not evolve with time.

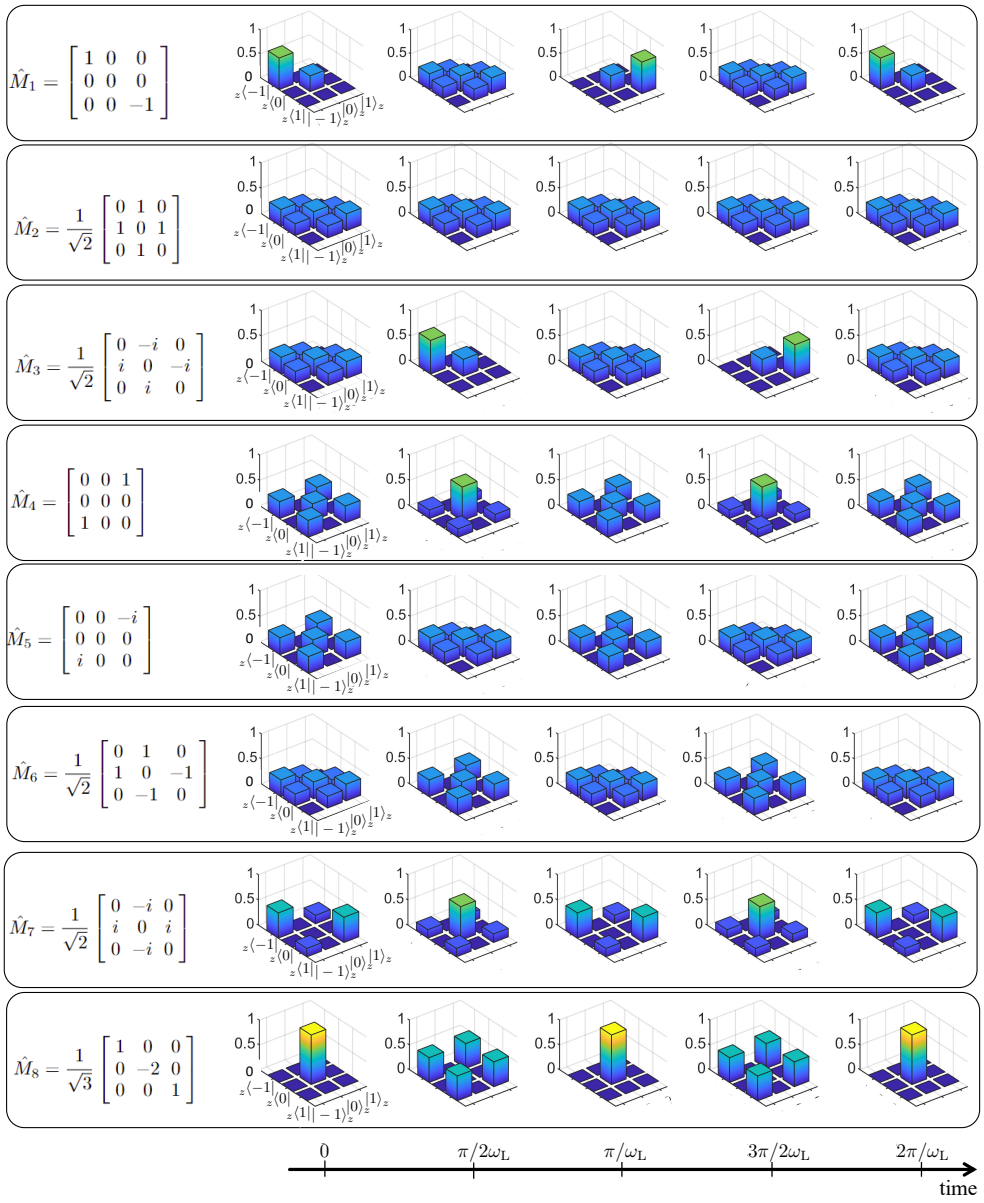

Figure 2. Time evolution of the density matrix in the transverse magnetic field with 8 different initial conditions including $\hat{M}_1 \cdots \hat{M}_8$. The bars correspond to the moduli of the density matrix elements. To clearly show the oscillation, $\hat{M}_7$ is shifted in time by $\pi/4\omega_L$.

Moreover, if one focuses for example on the population difference between $|-1\rangle_z$ and $|1\rangle_z$, which is at the origin of the spin noise signal in a standard SNS configuration (see the following sections), one notices that only mechanisms corresponding to $i = 1, 3$ lead to an oscillation of this population difference. This means that, in a standard SNS configuration, only one noise peak at ω_L will be observed.

Such a discussion, which is particularly simple in the case of the standard far detuned SNS configuration in which one observes the Faraday rotation noise with a transverse magnetic field, will be extended to more exotic configurations in the next sections, then involving all the different processes of Fig. 2.

III. CASE OF A $J = 1 \rightarrow J = 0$ TRANSITION

As can be seen in Fig. 1, the ^{4}He level structure allows to probe the spin noise of the 2^3S_1 level (which has $J = 1$) using three well separated transitions. One can thus choose an upper level with a total angular momentum $J = 0, 1$, or 2. The optical consequences of the different spin noise mechanisms of Fig. 2 on the probe light polarization are thus expected to depend on the transition. We start in the present section by considering the simplest case of the $J = 0$ upper level (D_0 line), which has been experimentally and theoretically described in details in Ref. [17].

Like in standard SNS experiments [4], we suppose here that i) the sample is probed using *linearly polarized light* and ii) the probe light is *far detuned from resonance*, so that absorption and dichroism can be

neglected [, Liu2022] while the only relevant effects are those linked to the *refractive index* of the vapor. Two kinds of birefringences must then be considered, leading to orientation or ellipticity fluctuations in the polarization of the probe beam.

A. Spin noise detected as circular birefringence

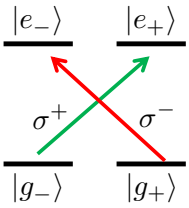

Figure 3. The simplified spin-$\frac{1}{2}$ model. [12]

The first type of fluctuating birefringence that can be created by spin noise is circular birefringence (CB), leading to Faraday rotation for the probe light. It can be well explained using the simplified spin-1/2 model shown in Fig. 3. It corresponds to a relative phase difference between the two circularly polarized components of the probe light, which interact with two different transitions. Thus each circularly polarized component probes the population of one of the two ground state sublevels $|g_-\rangle$ and $|g_+\rangle$ [13]. This simplified picture remains valid in the case of our $J = 1 \rightarrow J = 0$ transition [10, 17, 24], as can be seen in Fig. 4(a) as a linearly polarized light propagating along z can only probe the populations of sublevels $|-1\rangle_z$ and $|+1\rangle_z$. A fluctuating population imbalance between these two sublevels leads to a fluctuating Faraday rotation (FR), whose observation is independent of the relative angle between the incident linear polarization direction and the magnetic field.

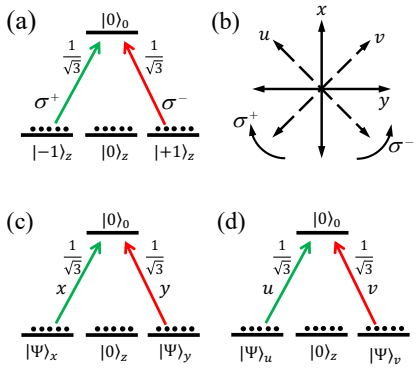

Figure 4. Level structure of the D_0 line. (a) Circular representation with quantization axis along z. (b) The two different linear basis for light polarization. (c) Linear x/y representation, the ground levels are coupled to the excited state by $\hat{x}$ or $\hat{y}$ polarization components. (d) In linear u/v representation, the ground levels are coupled to the excited state by $\hat{u}$ or $\hat{v}$ polarization components.

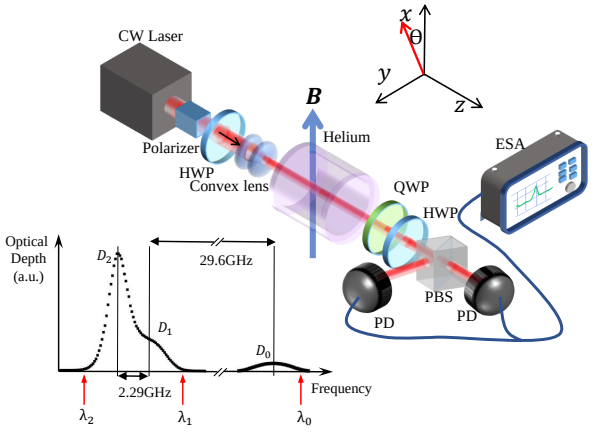

Figure 5. Experimental setup. The quarter-wave plate QWP is inserted after the cell to detect ellipticity noise and removed to detect rotation noise. HWP: half-wave plate, PD: photodetector, PBS: polarization beam-splitter, ESA: electronic spectrum analyzer. Inset: typical optical depth spectrum of the ^{4}He cell showing the three wavelengths used in this paper.

This isotropy of FR noise is confirmed by experiments performed with the set-up schematized in Fig. 5, without the quarter-wave plate. A radiofrequency discharge at 27 MHz is applied to a 6 cm long ^{4}He cell filled at 1 Torr, in order to populate the metastable 2^3S_1 state with a density of the order of 2×10^{11} cm^{-3} [17]. The linearly polarized laser light at 1.083 μm (CYFL-Kilo ultra low noise Keopsys fiber laser) is 1.5 GHz blue detuned from the D_0 line, and collimated to form a 0.6 mm diameter beam in the cell. A transverse uniform magnetic field is applied along x (Voigt geometry) using Helmholtz coils. The transmitted light carrying the spin noise information is then polarization analyzed using a half-wave plate followed by a polarization beamsplitter and a balanced detection. Adding a quarter-wave plate before the PBS permits to probe the ellipticity noise instead of the FR noise.

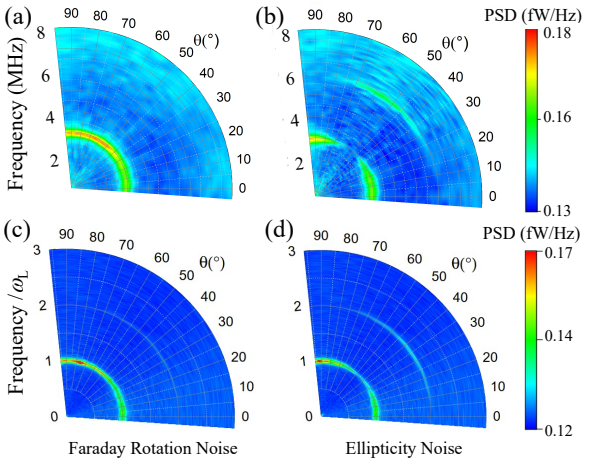

Figure 6. PSD of (a,c) FR noise and (b,d) ellipticity noise for various values of the angle θ. (a,b) Experiments performed with the probe frequency blue detuned by 1.5GHz from the D_0 line. (c,d) Corresponding simulations. The laser power is 1.5 mW.

The experimental results reproduced in Fig. 6(a) show the evolution of the Faraday rotation noise spectra as a function of the angle θ between the probe polarization and the direction x of the magnetic field. They confirm that, as expected from the preceding discussion and from the mechanisms $\hat{M}_1$ and $\hat{M}_3$ described in Fig. 2, one observes only one peak at the Larmor frequency $\omega_{\rm L}$ in the CB spin noise, and that this noise mode leads to an isotropic effect, independent of θ.

This result is in agreement with the theoretical predictions reproduced in Fig. 6(c), obtained by numerically simulating the evolution of the density matrix of the system, and explained in more details in Ref. [17]. It can also be confirmed by plotting the evolution of the population difference $n_{-1} - n_1 = {}_z\langle -1|\,\rho\,|-1\rangle_z - {}_z\langle 1|\,\rho\,|1\rangle_z$ between levels $|-1\rangle_z$ and $|+1\rangle_z$, as shown in Fig. 7(a): when FR noise is detected, only the frequency $\omega_{\rm L}$ is excited whatever the value of θ.

B. Spin noise detected as linear birefringence

Apart from Faraday rotation fluctuations, the spin noise can give rise to a fluctuating linear birefringence (LB), leading to an ellipticity noise for the probe beam. One main difference between a LB and a CB is that a LB has neutral axes, which can have various orientations with respect to the x and y directions. We thus decompose LB noise into two components: LB with neutral axes oriented along x and y, and LB with neutral axes oriented along the directions u and v of Fig. 4(b), which are rotated by $\pi/4$ with respect to x and y. The relations between the unit vectors along those different directions are given by

$$\hat{\sigma}^+ = (\hat{x} + i\hat{y})/\sqrt{2}\ , \tag{11}$$

$$\hat{\sigma}^- = (\hat{x} - i\hat{y})/\sqrt{2}\ , \tag{12}$$

and

$$\hat{u} = (\hat{x} - \hat{y})/\sqrt{2}\ , \tag{13}$$

$$\hat{v} = (\hat{x} + \hat{y})/\sqrt{2}\ . \tag{14}$$

In order to better understand the optical noise signals corresponding to these LB fluctuations, we consider the natural basis for the sublevels of the ground state of the transition in the cases of the x/y-oriented and u/v-oriented LB. In the first case, the sublevels, which are coupled to the excited state by $x-$ and $y-$ polarized light are, respectively:

$$|\Psi_x\rangle = \frac{1}{\sqrt{2}}(|-1\rangle_z + |+1\rangle_z), \tag{15}$$

$$|\Psi_y\rangle = -\frac{i}{\sqrt{2}}(|-1\rangle_z - |+1\rangle_z)\ . \tag{16}$$

In the case of the u/v LB, the sublevels that are coupled by light polarized along the u and v directions (see Fig. 4(b)) are respectively given by

$$|\Psi_u\rangle = \frac{1}{\sqrt{2}}(e^{i\pi/4}\,|-1\rangle_z + e^{-i\pi/4}\,|+1\rangle_z))\ , \tag{17}$$

$$|\Psi_v\rangle = \frac{1}{\sqrt{2}}(e^{-i\pi/4}\,|-1\rangle_z + e^{i\pi/4}\,|+1\rangle_z)\ . \tag{18}$$

It happens that $\hat{M}_4$, $\hat{M}_7$ and $\hat{M}_8$ are diagonal in the $\{|\Psi_x\rangle, |0\rangle_z, |\Psi_y\rangle\}$ basis, while it is the case for $\hat{M}_5$ and $\hat{M}_6$ in the $\{|\Psi_u\rangle, |0\rangle_z, |\Psi_v\rangle\}$ basis. Similarly to Fig. 7(a), Figs. 7(b) and 7(c) show the evolutions of the population differences

$$n_x - n_y = \langle\Psi_x|\,\rho\,|\Psi_x\rangle - \langle\Psi_y|\,\rho\,|\Psi_y\rangle\ , \tag{19}$$

$$n_u - n_v = \langle\Psi_u|\,\rho\,|\Psi_u\rangle - \langle\Psi_v|\,\rho\,|\Psi_v\rangle\ , \tag{20}$$

respectively for the noise mechanisms $\hat{M}_4$, $\hat{M}_7$, $\hat{M}_8$ on the one hand, and $\hat{M}_5$ and $\hat{M}_6$ on the other hand.

From Fig. 7(b), one can see that the observation of linear birefringence along the x/y orientation must lead to the appearance of spin noise only at frequency $2\omega_{\rm L}$, because the three mechanisms $\hat{M}_4$, $\hat{M}_7$, $\hat{M}_8$ oscillate at this frequency. In contrast, Fig. 7(c) shows that the ellipticity noise components observable along the u/v directions correspond to mechanisms $\hat{M}_5$ and $\hat{M}_6$, which evolve at frequency $\omega_{\rm L}$ only.

These predictions are summarized in Table I. They are also confirmed by Fig. 8, which shows the evolution, in their respective eigenbasis, of the moduli of the density matrix elements for the five mechanisms of Figs. 7(b) and 7(c) that contribute to ellipticity noise.

Table I. Different noise mechanisms corresponding to different detection strategies and different types of fluctuating birefringences for the D_0 transition.

Noise type	Faraday rotation	Ellipticity	
Birefringence type	Circular birefringence	x/y Linear birefringence	u/v Linear birefringence
Mechanisms	$\hat{M}_1, \hat{M}_3$	$\hat{M}_4, \hat{M}_7, \hat{M}_8$	$\hat{M}_5, \hat{M}_6$
Frequency	$\omega_{\rm L}$	$2\omega_{\rm L}$	$\omega_{\rm L}$

Finally, these predictions are fully verified by the experimental results of Fig. 6(b) and the simulations of Fig. 6(d). They explain why only spin noise at frequency $\omega_{\rm L}$ can be detected in the ellipticity noise with $\theta = 0$ and $\theta = \pi/2$ [mechanisms $\hat{M}_5$ and $\hat{M}_6$ of Figs. 7(c) and 8, which have neutral axes along u and v] and why only spin noise at frequency $2\omega_{\rm L}$ can be detected in the ellipticity noise with $\theta = \pi/4$ [mechanisms $\hat{M}_4$, $\hat{M}_7$ and $\hat{M}_8$ of Figs. 7(b) and 8, which have neutral axes along x and y].

Finally, let us stress the fact that when the polarization direction θ is changed, this does not change the amplitude of the different spin noise mechanisms, which are always present, but only the way they can be detected or not.

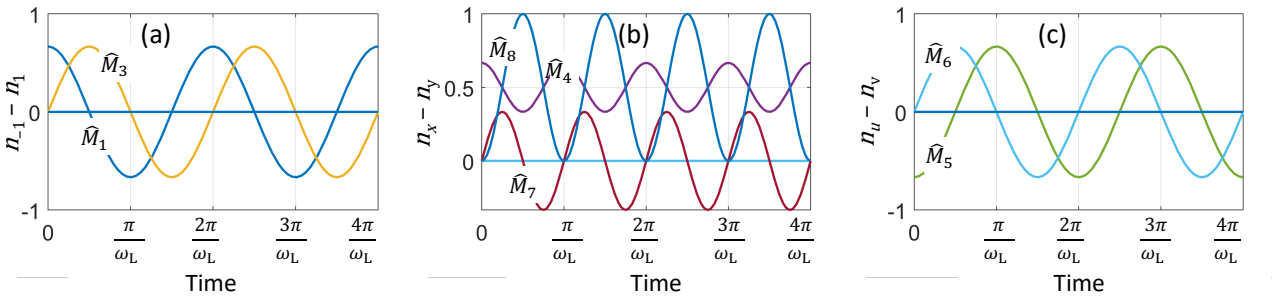

Figure 7. Time evolution of the population difference between states (a) $|-1\rangle_z$ and $|1\rangle_z$, (b) $|\Psi_x\rangle$ and $|\Psi_y\rangle$, and (c) $|\Psi_u\rangle$ and $|\Psi_v\rangle$ for different mechanisms.

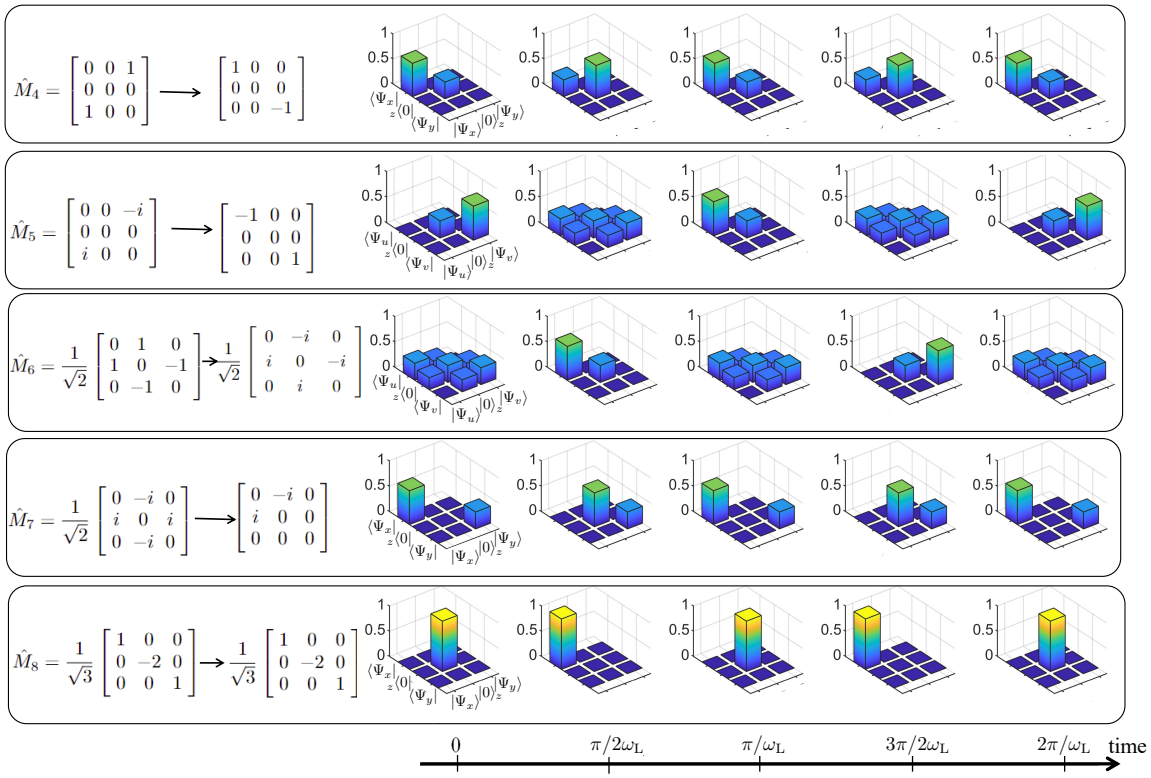

Figure 8. Same as Fig. 2 for the mechanisms $\hat{M}_4$, $\hat{M}_5$, $\hat{M}_6$, $\hat{M}_7$, and $\hat{M}_8$, represented in another basis. The evolution of the density matrix for mechanisms $\hat{M}_4$, $\hat{M}_7$, and $\hat{M}_8$ (respectively $\hat{M}_5$ and $\hat{M}_6$) is shown in the x/y (respectively u/v) representation.

IV. CASES OF D_1 AND D_2 TRANSITIONS

In this section, the discussion of the observation of the different spin noise modes is extended to the two other lines of metastable helium, namely the $J = 1 \rightarrow J = 1$ and $J = 1 \rightarrow J = 2$ transitions (so-called D_1 and D_2 lines). Figures 9(a) and 10(a) show the corresponding sublevel structures with the quantization axis oriented along z, together with the Clebsch-Gordan coefficients of the associated transitions. By comparison with the $J = 1 \rightarrow J = 0$ transition investigated in the preceding section (see Fig. 4(a)), one can see that the D_1 and D_2 lines are much more complicated. Understanding how the spin noise modes of Fig. 2 can be observed either as FR noise or as ellipticity noise thus requires a bit more formalism than in the case of the D_0 line. As the linear absorption of these transitions is larger than for the D_0 line, the probe laser is now detuned by 2 GHz: the remaining absorption then remains below 5%, so that the back action of the probe can be neglected as shown in a previous work [17].

A. Spin noise detected as circular birefringence

We start in this section by comparing the Faraday rotation noise for the D_1 and D_2 lines with the one for the D_0 line discussed in Section III A. To this aim, the optical couplings between the sublevels of the lower and upper levels of the different transitions, schematized in Figs. 4(a), 9(a), and 10(a) are represented as matrices. For example, for the D_0 line, the Clebsch-Gordan coefficients representing the coupling by σ^+-polarized

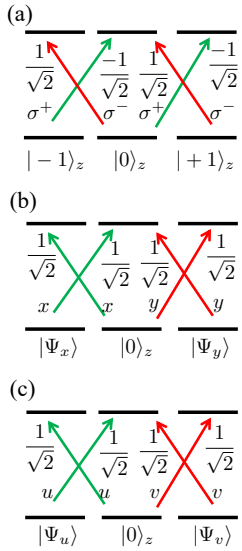

Figure 9. Sublevel structure of the levels of the D_1 transition. (a) In circular representation. (b) In linear x/y representation. (c) In linear u/v representation. Notice that the three sublevels of the upper level of the transition are different in the three representations.

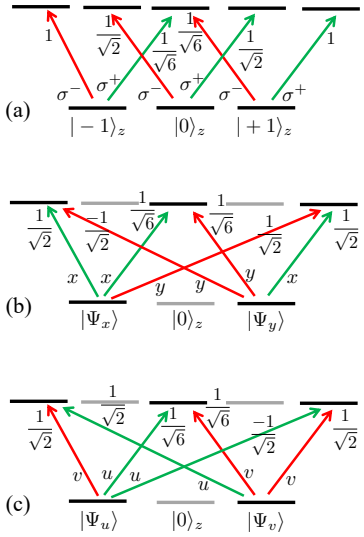

Figure 10. Same as Fig. 9 for the D_2 line. The transitions between the gray sublevels are not shown because they are coupled with equal Clebsch-Gordan coefficients for the two polarizations (x and y in (b) or u and v in (c)) and thus do not contribute to any linear birefringence.

light between the two levels read

$$\Gamma_0^{(+)} = \begin{bmatrix} \frac{1}{\sqrt{3}} \\ 0 \\ 0 \end{bmatrix}, \tag{21}$$

where the three rows correspond to the three sublevels $|-1\rangle_z$, $|0\rangle_z$, and $|+1\rangle_z$ of the ground state and the single column to the non degenerate upper level. Similarly, the coupling matrix for σ^--polarized light reads

$$\Gamma_0^{(-)} = \begin{bmatrix} 0 \\ 0 \\ \frac{1}{\sqrt{3}} \end{bmatrix}. \tag{22}$$

Further, the coupling matrices for the D_1 line read

$$\Gamma_1^{(+)} = -\frac{1}{\sqrt{2}} \begin{bmatrix} 0 & 1 & 0 \\ 0 & 0 & 1 \\ 0 & 0 & 0 \end{bmatrix}, \Gamma_1^{(-)} = \frac{1}{\sqrt{2}} \begin{bmatrix} 0 & 0 & 0 \\ 1 & 0 & 0 \\ 0 & 1 & 0 \end{bmatrix}, \tag{23}$$

where the columns refer to the excited state of the D_1 line with the quantization axis oriented along z. Finally, in the case of the D_2 line, we have:

$$\Gamma_2^{(+)} = \begin{bmatrix} 0 & 0 & \frac{1}{\sqrt{6}} & 0 & 0 \\ 0 & 0 & 0 & \frac{1}{\sqrt{2}} & 0 \\ 0 & 0 & 0 & 0 & 1 \end{bmatrix}, \tag{24}$$

$$\Gamma_2^{(-)} = \begin{bmatrix} 1 & 0 & 0 & 0 & 0 \\ 0 & \frac{1}{\sqrt{2}} & 0 & 0 & 0 \\ 0 & 0 & \frac{1}{\sqrt{6}} & 0 & 0 \end{bmatrix}, \tag{25}$$

where the columns correspond to the Zeeman sublevels of the excited state of D_2.

By comparing Figs. 9(a) and 10(a) with Fig. 4(a), one can predict the behavior of FR spin noise when the laser is tuned close to the D_1 and D_2 transitions. The difference between the D_1 and D_2 lines, on the one hand, and the D_0 line, on the other hand, is that the state $|0\rangle_z$ is now coupled to the the upper level by σ^+ and σ^--polarized light, with the same Clebsch-Gordan coefficients. This means that a fluctuation of the population of this state will induce the same variations of the refractive indices seen by the σ^+ and σ^- polarizations, and will thus not induce any FR. Consequently, some FR noise can be induced only by an imbalance between the populations of the states $|-1\rangle_z$ and $|1\rangle_z$. Figure 9(a) shows that for the D_1 line the situation is the same as for the D_0 line: state $|-1\rangle_z$ affects only σ^+-polarized light while state $|1\rangle_z$ affects only σ^--polarized light. FR rotation noise should thus be the same for D_1 and D_0 line. The situation is slightly different for the D_2 line: Figure 10(a) shows that both states $|-1\rangle_z$ and $|1\rangle_z$ are coupled to the upper level by both σ^+ and σ^--polarized light. But the 1:6 ratio between the transitions strengths shows that again state $|-1\rangle_z$ is coupled to the upper level mainly by σ^+-polarized light while state $|1\rangle_z$ is sensitive mainly to σ^--polarized light. We thus expect again FR noise for the D_2 line to be very similar to the one for the D_0 and D_1 lines.

These predictions are perfectly confirmed by both the numerical simulations and the experimental results. Figures 11(a) and 11(c) show the measured FR noise spectra for a laser frequency detuned from the D_1 and D_2 lines respectively. Figures 12(a) and 12(c) are the corresponding simulations. In each case, like in the case of the D_0 line (see Figs. 6(a) and 6(c)), only the noise peak at ω_L is visible, with an intensity almost independent from θ.

One can notice that the experimental CB spin noise spectra are weaker for the D_1 line than for the two other lines. The first reason is that the D_1 line is weaker than the D_2 line (see Fig. 5). But another reason behind this can be deduced from the simulations of Fig. 13. This figure shows the evolution of the Faraday rotation versus time, in the presence of

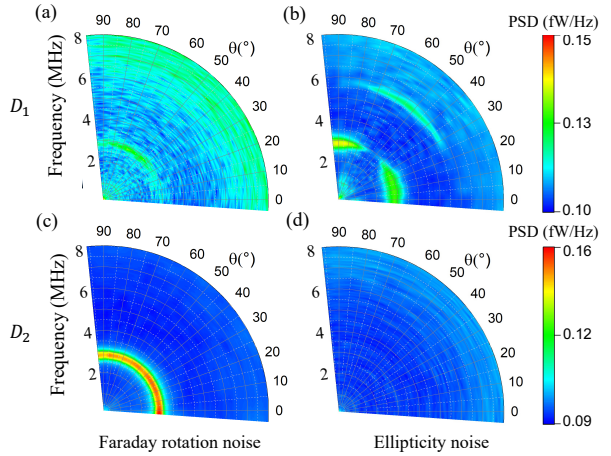

Figure 11. Experimental spin noise spectra for FR noise (left column) and ellipticity noise (right column). (a,b) Laser blue detuned by 2 GHz from the D_1 line; (c,d) Laser red detuned by 2 GHz from the D_2 line. Laser power: 1.5 mW

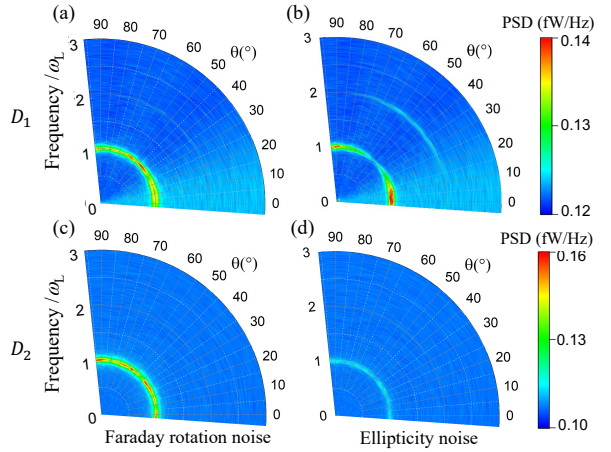

Figure 12. Simulated spin noise spectra corresponding to the measurements of Fig. 11. The parameters of the simulations are taken from the experiment.

the transverse magnetic field, when mechanisms $\hat{M}_1$ (Fig. 13(a)) and $\hat{M}_3$ (Fig. 13(b)) are excited at $t = 0$. These two mechanisms, which are responsible for the FR noise at frequency ω_L, are simulated for the three lines and shows that the amplitude of Faraday rotation is approximately the same for the D_1 and D_2 lines for the same initial conditions. However, the signal induced by the D_2 line is out of phase with respect to the ones induced by D_0 and D_1 lines. This phase shift also contributes to reduce the FR noise observed close to the D_1 line, because it contains some signal with the opposite sign coming from the nearby intense D_2 line. This destructive interference effect among the spin noise signals coming from the two transitions further contributes to reducing the FR noise.

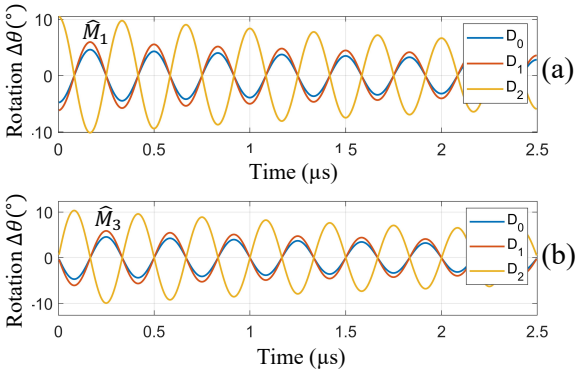

Figure 13. Time evolution of the probe polarization rotation close to the D_0, D_1, and D_2 lines for initial conditions corresponding to (a) mechanism $\hat{M}_1$ and (b) mechanism $\hat{M}_3$.

B. Spin noise detected as linear birefringence

The prediction of the behavior of the ellipticity noise for the D_1 and D_2 lines can be performed in a manner similar to Section III B, i.e., by changing the basis of the lower level from $\{|-1\rangle_z, |0\rangle_z, |1\rangle_z\}$ to some more relevant basis $\{|\Psi_x\rangle, |0\rangle_z, |\Psi_y\rangle\}$ or $\{|\Psi_u\rangle, |0\rangle_z, |\Psi_v\rangle\}$. However, since the upper levels of these two transitions also exhibit several sublevels, this change of basis for the lower level depends on the considered transition. Moreover, one must also perform a change of basis for the upper level in order to isolate the different transitions corresponding to the different states of light polarization of Fig. 4(b).

Consequently, the coupling matrices corresponding to the ellipticity noise in the x/y and u/v basis read

$$\Gamma_i^{(x/y)} = M_{\mathrm{g},i}^{(x/y)}\, \Gamma_i\, M_{\mathrm{e},i}^{(x/y)}\,, \tag{26}$$

where $i = 0, 1, 2$ denotes the three different transitions with their corresponding upper levels, and where $M_{\mathrm{g,i}}^{(x/y)}$ and $M_{\mathrm{e},i}^{(x/y)}$ are the matrices for the change of basis for the ground and excited levels of the transition, respectively. A relation similar to Eq. (26) holds for the u/v basis.

The expressions of the matrices for the change of basis are given by

$$M_{\mathrm{g},0}^{(x/y)} = \frac{1}{\sqrt{2}} \begin{bmatrix} 1 & 0 & 1 \\ 0 & \sqrt{2} & 0 \\ -i & 0 & i \end{bmatrix}\,, \tag{27}$$

$$M_{\mathrm{g},0}^{(u/v)} = \frac{1}{2} \begin{bmatrix} 1+i & 0 & 1-i \\ 0 & 2 & 0 \\ 1-i & 0 & 1+i \end{bmatrix}\,, \tag{28}$$

$$M_{\mathrm{e},0}^{(x/y)} = M_{\mathrm{e},0}^{(u/v)} = [1]\,, \tag{29}$$

for the D_0 line,

$$M_{\mathrm{g},1}^{(x/y)} = \frac{1}{\sqrt{2}} \begin{bmatrix} -1 & 0 & 1 \\ 0 & \sqrt{2} & 0 \\ i & 0 & i \end{bmatrix} , \tag{30}$$

$$M_{\mathrm{g},1}^{(u/v)} = \frac{1}{2} \begin{bmatrix} -1-i & 0 & 1-i \\ 0 & 2 & 0 \\ -1+i & 0 & 1+i \end{bmatrix} , \tag{31}$$

$$M_{\mathrm{e},1}^{(x/y)} = \frac{1}{\sqrt{2}} \begin{bmatrix} 1 & 0 & i \\ 0 & \sqrt{2} & 0 \\ -1 & 0 & i \end{bmatrix} , \tag{32}$$

$$M_{\mathrm{e},1}^{(u/v)} = \frac{1}{2} \begin{bmatrix} 1-i & 0 & 1+i \\ 0 & 2 & 0 \\ -1-i & 0 & -1+i \end{bmatrix} , \tag{33}$$

for the D_1 line, and

$$M_{\mathrm{g},2}^{(x/y)} = M_{\mathrm{g},0}^{(x/y)} , \tag{34}$$

$$M_{\mathrm{g},2}^{(u/v)} = M_{\mathrm{g},0}^{(u/v)} , \tag{35}$$

$$M_{\mathrm{e},2}^{(x/y)} = \frac{1}{\sqrt{2}} \begin{bmatrix} 1 & 0 & 0 & 0 & i \\ 0 & 1 & 0 & i & 0 \\ 0 & 0 & \sqrt{2} & 0 & 0 \\ 0 & 1 & 0 & -i & 0 \\ 1 & 0 & 0 & 0 & -i \end{bmatrix} , \tag{36}$$

$$M_{\mathrm{e},2}^{(u/v)} = \frac{1}{2} \begin{bmatrix} \sqrt{2} & 0 & 0 & 0 & i\sqrt{2} \\ 0 & 1-i & 0 & 1+i & 0 \\ 0 & 0 & 2 & 0 & 0 \\ 0 & 1+i & 0 & 1-i & 0 \\ \sqrt{2} & 0 & 0 & 0 & -i\sqrt{2} \end{bmatrix} , \tag{37}$$

for the D_2 line.

Using these transformation matrices in Eq. (26), the coupling matrices in these linear basis become

$$\Gamma_0^{(x)} = \Gamma_0^{(u)} = \begin{bmatrix} \frac{1}{\sqrt{3}} \\ 0 \\ 0 \end{bmatrix} , \tag{38}$$

$$\Gamma_0^{(y)} = \Gamma_0^{(v)} = \begin{bmatrix} 0 \\ 0 \\ \frac{1}{\sqrt{3}} \end{bmatrix} , \tag{39}$$

for the D_0 line. They confirm the branching ratios represented in Figs. 4(b) and 4(c) and the results discussed in Section III B.

For the D_1 line, the coupling matrices become

$$\Gamma_1^{(x)} = \Gamma_1^{(u)} = \frac{1}{\sqrt{2}} \begin{bmatrix} 0 & 1 & 0 \\ 1 & 0 & 0 \\ 0 & 0 & 0 \end{bmatrix} , \tag{40}$$

$$\Gamma_1^{(y)} = \Gamma_1^{(v)} = \frac{1}{\sqrt{2}} \begin{bmatrix} 0 & 0 & 0 \\ 0 & 0 & 1 \\ 0 & 1 & 0 \end{bmatrix} , \tag{41}$$

which are summarized in Figs. 9(b) and 9(c). Finally, for the D_2 line, these matrices read

$$\Gamma_2^{(x)} = \begin{bmatrix} \frac{1}{\sqrt{2}} & 0 & \frac{1}{\sqrt{6}} & 0 & 0 \\ 0 & \frac{1}{\sqrt{2}} & 0 & 0 & 0 \\ 0 & 0 & 0 & 0 & \frac{1}{\sqrt{2}} \end{bmatrix} , \tag{42}$$

$$\Gamma_2^{(y)} = \begin{bmatrix} 0 & 0 & 0 & 0 & \frac{1}{\sqrt{2}} \\ 0 & 0 & 0 & \frac{1}{\sqrt{2}} & 0 \\ -\frac{1}{\sqrt{2}} & 0 & \frac{1}{\sqrt{6}} & 0 & 0 \end{bmatrix} , \tag{43}$$

and

$$\Gamma_2^{(u)} = \begin{bmatrix} 0 & 0 & \frac{1}{\sqrt{6}} & 0 & -\frac{1}{\sqrt{2}} \\ 0 & \frac{1}{\sqrt{2}} & 0 & 0 & 0 \\ \frac{1}{\sqrt{2}} & 0 & 0 & 0 & 0 \end{bmatrix} , \tag{44}$$

$$\Gamma_2^{(v)} = \begin{bmatrix} \frac{1}{\sqrt{2}} & 0 & 0 & 0 & 0 \\ 0 & 0 & 0 & \frac{1}{\sqrt{2}} & 0 \\ 0 & 0 & \frac{1}{\sqrt{6}} & 0 & \frac{1}{\sqrt{2}} \end{bmatrix} . \tag{45}$$

These branching ratios are shown in Figs. 10(b) and 10(c), except for the gray levels of Figs. 10(b) and 10(c), which are coupled with equal Clebsch-Gordan coefficients for the two polarizations and thus do not contribute to any linear birefringence.

By comparing Figs. 4(c), 9(b), and 10(b), we can predict that the ellipticity noise detected in the vicinity of the D_2 line should be strongly different from the one detected close to the D_0 and D_1 lines. Indeed, Figs. 4(c) and 9(b) show that for the D_0 and D_1 lines, the states $|\Psi_x\rangle$ and $|\Psi_y\rangle$ are respectively coupled to the upper level by $x-$ and $y-$ polarized light *only*. On the contrary, in the case of the D_2 line, the states $|\Psi_x\rangle$ and $|\Psi_y\rangle$ are always coupled to the upper level by *both* $x-$ and $y-$ polarized light. For example, according to the coupling coefficients of Fig. 10(b) and Eqs. (42) and (43), the state $|\Psi_x\rangle$ is coupled to the upper level by $x-$ and $y-$ polarized light with probabilities respectively proportional to 2/3 and 1/2, which are quite close. This means that the fluctuating LB created by mechanisms $\hat{M}_4$, $\hat{M}_7$, and $\hat{M}_8$ of Fig. 2 and originating from an imbalance $n_x - n_y$ between the populations of states $|\Psi_x\rangle$ and $|\Psi_y\rangle$ will lead to a much weaker LB in the case of the D_2 line than in the case of the D_0 and D_1 line. Moreover, we predict that the associated ellipticity noise at frequency $2\omega_{\mathrm{L}}$ will be smaller and also less polarization sensitive in the vicinity of the D_2 line.

This conclusion also holds for the component of LB noise with its neutral axes oriented along the u and v directions of Fig. 4(b). Comparison of Figs. 4(d), 9(c), and 10(c) again shows that in this case the ellipticity noise at frequency ω_{L}, corresponding to mechanisms $\hat{M}_5$ and $\hat{M}_6$ of Fig. 2, should behave similarly in the vicinity of the D_0 and D_1 lines but be much weaker and less polarization resolved for the D_2 line.

These expectations are confirmed by the measurements reproduced in Fig. 11 and the simulations of Fig. 12. Comparison with Figs. 6(b) and 6(d) shows indeed that the LB fluctuations of the D_1 line (Figs. 11(b) and 12(b)) are similar to the ones of the D_0 line. On

the contrary, in the vicinity of the D_2 line, the predicted signal (see Fig. 12(d)) is so weak that it becomes undetectable in the experiment (see Fig. 11(d)).

V. CONCLUSION

In this work, the noise modes of a spin-1 system in the presence of a magnetic field are investigated. The corresponding noises imprinted on the polarization of an initially linearly polarized probe light beam are studied in details, when the light is detuned from three different transitions corresponding to three different upper level structures. In all cases, both Faraday rotation and ellipticity noises, induced respectively by fluctuating circular and linear birefringences, are theoretically and experimentally analyzed.

Compared with conventional SNS that focuses on Faraday rotation noise only, the additionally detected ellipticity noise opens new windows on the system. Indeed, it permits to fully unveil the richer spin noise dynamics of high-spin systems. All put together, the detection of different spin noise signals for different orientations of the probe polarization permits to fully attribute the different components of the light polarization noise to different modes of oscillation of the spin state. As a consequence, although the polarization of the probe does not affect the spin noise itself, it has a strong influence on the spin noise signal when the probe laser effect on the atoms can be neglected.

Moreover, this paper illustrates the fact that, contrary to a commonly accepted idea, spin noise signals obtained with far detuned light do not depend only on the structure of the lower level of the transition: the structure of the upper level matters and can make the linear birefringence so weak that its effect is not visible anymore. Indeed, using metastable ^{4}He that exhibits three well separated lines starting from the same $J = 1$ lower level, both theory and experiments confirm that ellipticity and Faraday rotation noises behave differently and that the ellipticity noise resonances can be washed out in the vicinity of some transitions. This is explained by the way the different spin noise modes map to the polarization components of the probe light through the associated Clebsch-Gordan coefficients. Future work should also consider the behavior of these spin degrees of freedom when atoms are perturbed by an external field, whether light [25] or magnetic: as they might not couple to the perturbation in the same way, the spin resonances could more clearly depend on the transition.

The present work has benefited of the relatively simple level structure of ^{4}He, in which the different transitions are well separated in spite of Doppler broadening at room temperature. However, it opens interesting perspectives for even more complicated systems, such as alkali atoms, in which the spins of the levels are even larger, and in which the separation between hyperfine levels is very often smaller than the Doppler broadening. Indeed, generalizing the present approach to these more complicated atoms could allow to predict the conditions in which one can observe spin noise modes that are usually inaccessible.

Besides, the decomposition of spin noise of spin-1 system into eight different noise modes could be used to fully characterize the state of a spin-1 system by a tomographic technique based on this set of measurement modes [26, 27].

ACKNOWLEDGMENTS

The authors acknowledge funding by the Institut Universitaire de France, the Chinese Scholarship Council, and the Labex PALM.

[1] R. Hanbury-Brown and R. Q. Twiss, Nature **177**, 27 (1956).
[2] E. Aleksandrov and V. Zapasskii, Zh. Eksp. Teor. Fiz **81**, 132 (1981).
[3] E. B. Aleksandrov, Y. M. Golubev, A. V. Lomakin, and V. Noskin, Soviet Physics Uspekhi **26**, 643 (1983).
[4] S. A. Crooker, D. G. Rickel, A. V. Balatsky, and D. L. Smith, Nature **431**, 49 (2004).
[5] M. Oestreich, M. Römer, R. J. Haug, and D. Hägele, Phys. Rev. Lett. **95**, 216603 (2005).
[6] S. Crooker, J. Brandt, C. Sandfort, A. Greilich, D. Yakovlev, D. Reuter, A. Wieck, and M. Bayer, Physical review letters **104**, 036601 (2010).
[7] S. Cronenberger, D. Scalbert, D. Ferrand, H. Boukari, and J. Cibert, Nature Communications **6**, 8121 (2015).
[8] V. S. Zapasskii, A. Greilich, S. A. Crooker, Y. Li, G. G. Kozlov, D. R. Yakovlev, D. Reuter, A. D. Wieck, and M. Bayer, Physical Review Letters **110**, 176601 (2013).
[9] L. Yang, P. Glasenapp, A. Greilich, D. Reuter, A. D. Wieck, D. R. Yakovlev, M. Bayer, and S. A. Crooker, Nat. Comm. **5**, 4949 (2014).
[10] D. Roy, L. Yang, S. A. Crooker, and N. A. Sinitsyn, Scientific Reports **5**, 1 (2015).
[11] M. Swar, D. Roy, D. Dhanalakshmi, S. Chaudhuri, S. Roy, and H. Ramachandran, Opt. Express **26**, 32168 (2018).
[12] T. Mitsui, Physical review letters **84**, 5292 (2000).
[13] V. S. Zapasskii, Adv. Opt. Photon. **5**, 131 (2013).
[14] M. Glazov and V. Zapasskii, Optics Express **23**, 11713 (2015).
[15] A. A. Fomin, M. Y. Petrov, G. G. Kozlov, M. M. Glazov, I. I. Ryzhov, M. V. Balabas, and V. S. Zapasskii, Phys. Rev. Research **2**, 012008 (2020).
[16] G. Kozlov, A. Fomin, M. Y. Petrov, I. Ryzhov, and V. Zapasskii, Optics Express **29**, 4770 (2021).
[17] S. Liu, P. Neveu, J. Delpy, L. Hemmen, E. Brion, E. Wu, F. Bretenaker, and F. Goldfarb, New Journal of Physics **24**, 113047 (2022).
[18] B. P. Lanyon, M. Barbieri, M. P. Almeida, T. Jennewein, T. C. Ralph, K. J. Resch, G. J. Pryde, J. L. O'Brien, A. Gilchrist, and A. G. White, Nature Physics **5**, 134 (2009).
[19] P. B. Nisbet-Jones, J. Dilley, A. Holleczek, O. Barter, and A. Kuhn, New Journal of Physics **15**, 053007 (2013).
[20] A. R. Shlyakhov, V. V. Zemlyanov, M. V. Suslov,

A. V. Lebedev, G. S. Paraoanu, G. B. Lesovik, and G. Blatter, Phys. Rev. A **97**, 022115 (2018).
[21] V. Soltamov, C. Kasper, A. Poshakinskiy, A. Anisimov, E. Mokhov, A. Sperlich, S. Tarasenko, P. Baranov, G. Astakhov, and V. Dyakonov, Nature communications **10**, 1 (2019).
[22] D. Suter and T. Marty, J. Opt. Soc. Am. B **11**, 242 (1994).
[23] G. Colangelo, R. J. Sewell, N. Behbood, F. M. Ciurana, G. Triginer, and M. W. Mitchell, N. J. Phys. **15**, 103007 (2013).
[24] B. Mihaila, S. A. Crooker, D. G. Rickel, K. B. Blagoev, P. B. Littlewood, and D. L. Smith, Phys. Rev. A **74**, 043819 (2006).
[25] J. Delpy, S. Liu, P. Neveu, E. Wu, F. Bretenaker, and F. Goldfarb, Phys. Rev. A **107**, L011701 (2023).
[26] A. Kuzmich, L. Mandel, J. Janis, Y. E. Young, R. Ejnisman, and N. P. Bigelow, Phys. Rev. A **60**, 2346 (1999).
[27] T. Fernholz, H. Krauter, K. Jensen, J. F. Sherson, A. S. Sørensen, and E. S. Polzik, Phys. Rev. Lett. **101**, 073601 (2008).